SPE-175074-MS

Effect of Large Capillary Pressure on Fluid Flow and Transport in Stress-sensitive Tight Oil Reservoirs

Yi Xiong, Phil Winterfeld, and Cong Wang, Colorado School of Mines; Zhaoqin Huang, China University of Petroleum (East China); Yu-Shu Wu, Colorado School of Mines

This paper was prepared for presentation at the SPE Annual Technical Conference and Exhibition held in Houston, Texas, USA, 28–30 September 2015.

Abstract

The pore sizes of unconventional reservoir rock, such as shale and tight rock, are on the order of nanometers. The thermodynamic properties of in-situ hydrocarbon mixtures in such small pores are significantly different from those of fluids in bulk size, primarily due to effect of large capillary pressure. For example, it has been recognized that the phase envelop shifts and bubble-point pressure is suppressed in tight and shale oil reservoirs. On the other hand, the stress-dependency is pronounced in low permeability rocks. It has been observed that pore sizes, especially the sizes of pore-throats, are subject to decrease due to rock deformation induced by the fluid depletion from over-pressurized tight and shale reservoirs. This reduction on pore spaces again affects the capillary pressure and therefore thermodynamic properties of reservoir fluids. Thus it is necessary to model the effect of stress- dependent capillary pressure and rock deformation on tight and shale reservoirs.

In this paper, we propose and develop a multiphase, multidimensional compositional reservoir model to capture the effect of large capillary pressure on flow and transport in stress-sensitive unconventional reservoirs. The vapor-liquid equilibrium (VLE) calculation is performed with Peng-Robinson Equation of State (EOS), including the impact of capillary pressure on phase behavior and thermodynamic properties. The fluid flow is fully coupled with geomechanical model, which is derived from the thermo- poro-elasticity theory; mean normal stress as the stress variable is solved simultaneously with mass conservation equations. The finite-volume based numerical method, integrated finite difference method, is used for space discretization for both mass conservation and stress equations. The formulations are solved fully implicitly to assure the stability.

We use Eagle Ford tight oil formations as an example to demonstrate the effect of capillary pressure on VLE. It shows that the bubble-point pressure is suppressed within nano-pores, and fluid properties, such as oil density and viscosity, are influenced by the suppression due to more light components remained in liquid phase. In order to illustrate the effect of stress-dependent capillary pressure on tight oil flow and production, we perform numerical studies on Bakken tight oil reservoirs. The simulation results show that bubble-point suppression is exaggerated by effects of rock deformation, and capillary pressure on VLE also affects the reservoir pressure and effective stress. Therefore the interactive effects between capillary pressure and rock deformation are observed in numerical results. Finally, the production

performance in the simulation examples demonstrates the large effect of large capillary pressure on estimated ultimate recovery (EUR) in stress-sensitive tight reservoirs.

Introduction

Tight oil reservoirs have received great attention in recent years as one type of unconventional resources, because it is more economic than shale gas as well as technologies in horizontal drilling and massive hydraulic-fracturing advance. According to US Energy Information Administration (EIA, 2013a), tight oil is an industry convention that generally refers to oil produced from very-low- permeability shale, sandstone, and carbonate formations. Although the terms shale oil and tight oil are often used interchangeably in many contexts, shale formations are only a subset of all low-permeability tight formations. Thus tight oil is a more encompassing and accurate term with respect to the geologic formations producing oil than shale oil (EIA, 2013b). In this paper, a tight oil reservoir refers to a petroleum reservoir generally with very-low-permeability rocks, including shale plays, and an initial liquid-phase hydrocarbon fluid, i.e., a varying bubble-point system.

Characteristics of Tight Oil Reservoirs

A tight oil reservoir has some characteristics differentiating itself from a conventional petroleum reservoir, and the following characteristics are of interest to this paper.

Nano Pore Size and Ultra-low Permeability Tight oil reservoir rocks have very small pore and pore-throat sizes on the scale of nano-meters. For example, Kuila and Prasad (2011) point out that shale matrix has predominantly micro-pores with less than 2 nm diameter to meso-pores with 2-50 nm diameters. Nelson (2009) claims that the normal range of pore and pore-throat size for the shale matrix is from 5 to 50 nm, and provides the pore-throat size spectrum for different types of rocks.

Such small pore size, described above, results in ultra-low matrix permeability of tight oil reservoirs. Kurtoglu et al. (2014) tests the core plug permeability of Middle Bakken samples using the steady-state method with a supercritical fluid. It is found that the low, moderate and high permeability of Middle Bakken samples are 1.17×10^{-5} md, 6.27×10^{-4} md and 1.25×10^{-3} md, respectively.

High Initial Reservoir Pressure The current economically producing tight oil reservoirs have very high initial reservoir pressure. Overpressure is one of the key factors contributing to successful development of tight oil reservoirs. For example, Bakken tight oil reservoir has the pressure gradient up to 0.75 psi/ft and initial reservoir pressure could reach as high as 7,000 psi (Luneau et al., 2011) and even higher. Similarly Eagle Ford formation has initial reservoir pressure of about 7,500 psi at 10,500 feet TVD (true vertical depth) with a pressure gradient over 0.7 psi/ft (Deloitte, 2014). Wolfcamp shale in Permian basin also has pressure gradient up to 0.7 psi/ft and high initial reservoir pressure (Pioneer Natural Resource, 2013). Table 1 summarizes the pressure gradient and the common depth of pay zones of U.S. major tight oil formations.

Table 1—Summary of pressure gradient and depth of pay zones

Reservoirs	Pressure gradient (psi/ft)	TVD depth of pay zones (ft)
Eagle Ford	0.60 – 0.80	7,500-11,000 (oil window)
Bakken	0.45 – 0.75	9,000-11,000
Permian Wolfcamp Shale	0.55 – 0.75	5,500-11,000

Large Fraction of Light Components Another distinguishing feature of tight oil reservoirs is that the initial oil composition has a large molar fraction of light components. For example, the samples of Eagle Ford tight oil with low, medium and high gas solubility have molar fractions of light components (C1 and

C2) as high as 35%, 50% and 63% (Orangi et al., 2011); the Middle Bakken tight oil also has initial molar fraction of light components as high as 50% (Nojabaei et al., 2013; Wang et al., 2013).

Above characteristics lead to strong effects of pore confinement and rock compaction, shown in Figure 1. The small pore size and large fraction of light components result in significant pore confinement effect described in next section; rock compaction also plays a critical role, because it is hard or impossible to recharge the initial high pore pressure due to ultra-low permeability.

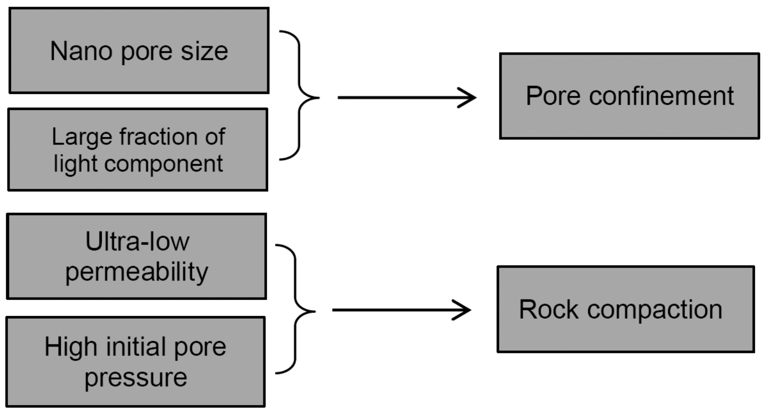

Figure 1—Characteristics of tight oil reservoirs and associated effects on flow behavoirs

Pore Confinement and Effect of Capillary Pressure on VLE

Such small pores of tight reservoir rocks lead to significant interfacial curvature and capillary pressure between confined vapor and liquid phases of hydrocarbons. According to Zarragoicoechea and Kuz (2004), there is a difference in thermodynamic phase behaviors for the fluids in small confined and large size pores. They point out that the phase behaviors and critical properties of the confined fluids must be altered as a function of the ratio of the molecule size to the pore size. Firincioglu et al. (2012) study the pore confinement effect on thermodynamic phase behaviors by including capillary pressure and surface forces in vapor-liquid equilibrium (VLE) calculation. It is found that the contribution of the surface forces is very small compared to the capillary force on the influence of phase behaviors; thus it is sufficient to represent the pore confinement effect by including the capillary pressure in VLE calculation.

Researchers have been investigating the impact of capillary pressure on fluid properties and phase behaviors since the 1970s in oil and gas industry. It was found that the dew-point and bubble-point pressure were same in the 30- to 40-US-mesh porous medium and in bulk volume (Sigmund et al., 1973), and concluded that capillary effects on VLE is negligible for conventional reservoirs. However, this assumption is not valid in general for tight oil reservoirs due to nano-scale pore sizes. It is recognized that bubble-point pressures of tight oil reservoirs are suppressed due to the capillary pressure. In other words, the fluid bubble point pressure with the same composition is lower in nanopores than measured in bulk size in PVT laboratory.

Since there is a large fraction of light components in oil composition discussed in above, the suppression on saturation pressure results in more light components remaining in oil phase instead of forming gas bubbles. Consequently the fluid properties, such as fluid density and viscosity, are also affected, and it further complicates the fluid flow behaviors.

Rock Compaction

Since there is a very high initial pore pressure, and it is hard or even impossible to maintain the initial pore pressure through fluid injection due to the ultra-low permeability, the decrease of pore pressure is substantial during the production for tight oil reservoirs. The large decrease of pore pressure, resulting in the increase of effective stress, further leads to the rock compaction.

The rock properties of tight oil reservoirs thus have a strong stress-dependency due to the influence of rock compaction. One of the major effects on rock properties is the degradation of absolute permeability. Chu et al. (2012) construct the compaction tables relating permeability reduction factor to the change of effective stress for Bakken tight oil reservoir based on laboratory measurements and history matches. Orangi et al. (2011) performe a simulation study for Eagle Ford tight oil reservoirs including the rock compaction effect and conclude that the transmissibility could decrease by an order of magnitude due to degradation of the fracture permeability.

Not only absolute permeability, other rock and fluid properties, such as porosity, relative permeability (Lai and Miskimins, 2010) and capillary pressure, etc., are also affected by rock compaction and deformation. Therefore, it is necessary to couple fluid flow and geomechanics in order to model rock compaction effect on the production performance for tight oil reservoirs.

Motivations

In addition to the effect of pore confinement or rock compaction, the interactions between them also exist. On one hand, the rock compaction could reduce the size of pores and pore-throats and further enlarge the pore confinement effect. On the other hand, the pore confinement effect, mainly the influence of capillary pressure on VLE, suppresses the oil saturation pressure and correspondingly affects fluid properties. Consequently, other reservoir properties, especially, pore pressure, are also affected by pore confinement effect during production. These influences resulting from pore confinement, in turn, affect the reservoir effective stress. Figure 2 illustrates that the tight oil modeling involves fluid flow, rock compaction, and pore confinement. In addition to interactions between pore confinement and rock compaction, fluid flow and rock compaction affect each other through the changes of pore pressure and stress-induced rock properties; pore confinement affects fluid flow through its effect on VLE.

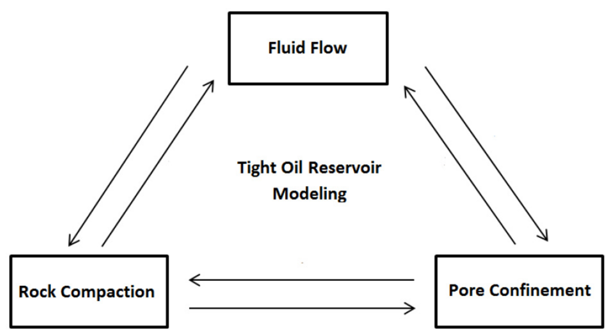

Figure 2—The processes involved in tight oil reservoir modeling

Thus this paper quantitatively investigates the effect of capillary pressure on VLE and rock compactions by developing a compositional model, which is fully coupled with geomechanics with its VLE calculation including the effect of capillary pressure. The mathematical model is addressed in next section; the VLE calculation method including capillarity effect is then discussed; finally two simulaton examples are presented to demonstrate effects of capillary pressure on fluid flow and production performance for a stress-senstive tight oil reservoir.

Mathematical Model

This section presents our mathematical model that discribes the physical processes of multiphase, multicomponent fluid flow coupled with geomechanical effects in tight oil reservoirs.

Compositional Model

A general compositional model is derived based on the law of mass conservation. Equation (1) is the governing mass balance equation for each mass component and the mass is evaluated by moles.

$$F_i + q_i = \frac{\partial N_i}{\partial t} \tag{1}$$

where subscript i is the index for mass component, $i = 1,...,n_c, n_w$ with n_c being the total number of hydrocarbon components; and n_w being the water component. Accumulation term, N_i, can be evaluated as follows by relating to phase molar density p, saturation $\boldsymbol{S}$, and component mole fraction in oil and gas phases $\boldsymbol{x_i}$ and $\boldsymbol{y_i}$.

$$N_i = \phi(\rho_o S_o x_i + \rho_g S_g y_i) \tag{2}$$

where $\boldsymbol{i = 1,...,n_c}$ donating hydrocarbon components and for water.

$$N_w = \phi \rho_w S_w \tag{3}$$

For tight oil and gas reservoirs, the mass flux from molecular diffusion of gas phase may not be negligible. Therefore for hydrocarbon component $\boldsymbol{i}$, its mass flux can be evaluated.

$$F_i = -\nabla \cdot \left(\rho_o x_i \vec{v}_o + \rho_g y_i \vec{v}_g\right) + \nabla \cdot \left(D_{eff,i} \nabla\left(\rho_g y_i\right)\right) \tag{4}$$

where the first term describes the advective mass flux from Darcy flow and the second term addresses the mass flux due to molecular diffusion in gas phase. The molecular diffusion in liquid phase is usually negligible compared to that in gas phase. In the second term, the molecular diffusion is driven by the concentration gradient. The effective diffusion coefficient of multiphase flow in a porous medium is in general a function of rock porosity and tortuosity. The mass flux of water component can be written as.

$$F_w = -\nabla \cdot \left(\rho_w \vec{v}_w\right) \tag{5}$$

$\vec{v}_\beta$ is Darcy velocity of liquid phase β, defined by Darcy's law for multiphase fluid flow as

$$\vec{v}_\beta = -\frac{k k_{r\beta}}{\mu_\beta}(\nabla P_\beta - \rho_\beta g \nabla Z) \tag{6}$$

where β is a phase index for gas, oil or water phase. For gas phase flow in tight reservoirs, the Klinkenberg effect (Klinkenberg, 1941) for gas permeability is included as follows.

$$k = k_\infty \left(1 + \frac{b_K}{P}\right) \tag{7}$$

Coupled Geomechanical Model

The coupled geomechanical model is derived based on the classical theory of poro-thermal-elastic system (Jaeger et al., 2007; Zoback, 2007), and the equilibrium equation can be expressed.

$$\sigma_{ij} - (\alpha P + 3\beta K \Delta T)\delta_{ij} = 2G\varepsilon_{ij} + \lambda \delta_{ij} \varepsilon_v \tag{8}$$

where volumetric strain ε_v is evaluated as:

$$\varepsilon_v = \varepsilon_{xx} + \varepsilon_{yy} + \varepsilon_{zz} \tag{9}$$

Another fundamental relation in the linear elasticity theory is the relationship between strain tensor and the displacement vector.

$$\varepsilon_{ij} = \frac{1}{2}\left(\frac{\delta u_i}{\delta x_j} + \frac{\delta u_j}{\delta x_i}\right) \tag{10}$$

And the condition of static equilibrium for a porous medium can be described as below.

$$\nabla \cdot \overline{\overline{\sigma}} + \overline{F_b} = 0 \tag{11}$$

Combine above equations to obtain the thermo-poro-elastic Navier's Equation as

$$\nabla(\alpha P+3\beta KT)+(\lambda+G)\nabla(\nabla\cdot\bar{u})+G\nabla^2\bar{u}+\bar{F}_b=0 \tag{12}$$

Above equation has two terms containing the displacement vector; taking the divergence of it results in the equation with only one term containing the divergence of the displacement vector. On the other hand, the trace of the stress tensor is an invariant with the same value for any coordinate system (Xiong, 2015). Finally we derive an equation relating mean stress, pore pressure, temperatures and body force:

$$\nabla\cdot[\nabla(\alpha P+3\beta KT)+\frac{\lambda+2G}{K}\nabla(\sigma_{mean}-\alpha P-3\beta K\Delta T)+\bar{F}_b]=0 \tag{13}$$

The temperature term can be neglected for the reservoir with the same initial temperature and following isothermal process during production. Thus above equations can be simplified as follows by removing temperature term for the tight oil reservoir.

$$\nabla\cdot[\nabla(\alpha P)+\frac{\lambda+2G}{K}\nabla(\sigma_{mean}-\alpha P)+\bar{F}_b]=0 \tag{14}$$

Above geomechanical model with the mean stress as the coupled variable has been successfully applied to other subsurface fluid systems. For example, Winterfeld and Wu (2015), Winterfeld et al. (2013) and Zhang (2013) have applied the mean stress formulation to simulate the geomechanical effect on CO_2 geological sequestration. Hu et al. (2013) and Xiong et al. (2013) also apply it to model the temperature- induced geomechanical effect for enhanced geothermal reservoirs.

Geomechanical Effect

The coupled geomechanics feeds back to fluid flow through its effects on reservoir properties.

Effective Stress Terzaghi (1936) initially defined the effective stress as the difference between normal stress and pore pressure, and Biot (1957) generalize it as:

$$\sigma'=\sigma_{mean}-\alpha P \tag{15}$$

Porosity and Permeability Reservoir porosity and absolute permeability are the functions of effective stress, especially for stresssensitive tight oil reservoirs. The general mathematical relations for can be expressed as:

$$\phi=\phi(\sigma') \qquad k=k(\sigma') \tag{16}$$

Mass Conservation The effect of geomechanics also influences the general mass conservation law of Equation (1). Firstly, the volume of a grid block is subjected to change due to rock deformation, which is incorporated into model by volumetric strain. Thus the accumulation term in Equation (1) should be evaluated as below to include volumetric strain for hydrocarbon component.

$$N_i=(1-\varepsilon_v)\phi\left(\rho_o S_o x_i+\rho_g S_g y_i\right) \tag{17}$$

In addition to accumulation term, the volumetric change also affects other geometric parameters, such as contact area and distances between grid blocks, which are essential to evaluate flux terms of mass balance equations.

Capillary Pressure The capillary pressure between oil and gas phases is critical to model tight oil reservoirs, because of its non-negligible effect on vapor-liquid equilibrium. It could be evaluated with well-known Young- Laplace equation (Equation (18)); the interfacial tension ***IFT*** could be estimated with composition data and Parachor values (Weinaug and Katz, 1943) as Equation (19), known as Macleod-Sugden correlation (Danesh, 1998).

$$P_c = \frac{2IFTcos\theta}{r} \tag{18}$$

$$IFT^{\frac{1}{4}} = \sum_{i=1}^{N_c} \chi_i \left(x_i \rho_o - y_i \rho_g \right) \tag{19}$$

where pore radius r is subjected to change due to rock deformation as a function of effective stress.

In addition, Leverett J-function (Leverett, 1940) can also be used to correct capillary pressure as follows.

$$P_c = P_{c0} \sqrt{\frac{k_0 \phi}{k \phi_0}} \tag{20}$$

where k_0 and k are initial permeability and stress-induced permeability, respectively; and ϕo and ϕ are porosities at initial and rock deformation states, respectively.

Discretized Governing Equations

The integral finite-difference (IFD) method (Narasimhan and Witherspoon, 1976; Pruess, 1991), a finite-volume based method, is employed for space discretization in this dissertation. Figure 3 shows the space discretization and geometry data in the IFD method.

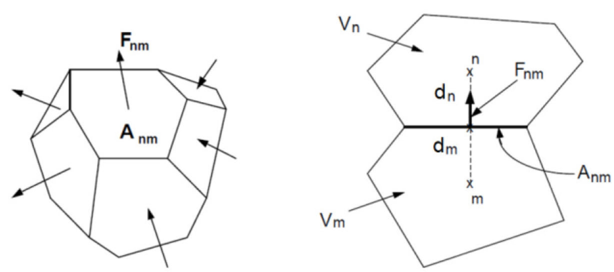

Figure 3—Space discretization and geometry data in the integral finite difference method (Pruess, 1991)

The left figure shows a grid block or arbitrary REV (representative elementary volume) V_n, and it has flux Fnm at each surface area A_{nm}; the right figure shows the geometry of two neighboring grid blocks, V_n and V_m, their interface A_{nm}, their distance to the interface d_n and d_m. With the IFD method, make volumetric integration and apply divergence theorem for the governing composition equation (Equation (1)) and geomechanical equation (Equation (14)) over REV, V_n, to obtain the following descritized equations. The time is discretized fully implicitly to assure numerical stability. For a hydrocarbon component:

$$\sum_{m \in \eta_n} [(\rho_o x_i \lambda_o)^{t+1}_{nm+\frac{1}{2}} \gamma^{t+1}_{nm} (\Psi^{t+1}_{om} - \Psi^{t+1}_{on}) + (\rho_g y_i \lambda_g)^{t+1}_{nm+\frac{1}{2}} \gamma^{t+1}_{nm} (\Psi^{t+1}_{gm} - \Psi^{t+1}_{gn})] + \sum_{m \in \eta_n} D_{eff,i} A^{t+1}_{nm} \frac{(\rho_g y_i)^{t+1}_m - (\rho_g y_i)^{t+1}_n}{d^{t+1}_n + d^{t+1}_m} + (Vq_i)^{t+1}_n$$
$$= \frac{\left[V\phi(\rho_o S_o x_i + \rho_g S_g y_i)\right]^{t+1}_n - \left[V\phi(\rho_o S_o x_i + \rho_g S_g y_i)\right]^t_n}{\Delta t} \tag{21}$$

where λ is the phase mobility defined as $\lambda = k_{r\beta/\mu\beta}$ for phase β Ψ is the flow potential including both pressure and gravity term; subscript *nm + 1/2* denotes a proper averaging at the interface between grid blocks *n* and *m;* η_n donates all neighboring grid blocks of *n; t + 1* is the current time step; and *t* is the previous time step; Γ is the transmissivity defined as

$$\gamma^{t+1}_{nm} = \left(\frac{A_{nm} k_{nm+\frac{1}{2}}}{d_n + d_m} \right)^{t+1} \tag{22}$$

For water component:

$$\sum_{m\in\eta_n}\left[(\rho_w\lambda_w)_{nm+\frac{1}{2}}^{t+1}\gamma_{nm}^{t+1}(\Psi_{wm}^{t+1}-\Psi_{wn}^{t+1})\right]+(Vq_w)_n^{t+1}=\frac{(V\phi\rho_w S_w)_n^{t+1}-(V\phi\rho_w S_w)_n^t}{\Delta t} \tag{23}$$

Different from the conventional fully implicit method, the geometry of grid blocks, such as the volume V_n, interface area A_{nm}, connection distances, d_n and d_m are subjected to change due to geomechanical effect. Thus those geometry variables and flow transmissivity Γ are evaluated at each Newton iteration of time step $t + 1$. The geomechanical governing equation can also be discretized with the IFD method as below.

$$\sum_{m\in\eta_n}\left[\frac{3(1-\nu)}{1+\nu}\frac{\sigma_n^{t+1}-\sigma_m^{t+1}}{d_{nm}}+(\bar{F}_b\cdot\hat{n})_{nm}-\frac{2\alpha(1-2\nu)}{1+\nu}\frac{P_n^{t+1}-P_m^{t+1}}{d_{nm}}\right]A_{nm}^{t+1}=0 \tag{24}$$

where the mean stress of grid blocks n and m is related with their reservoir pressures. Above discretized equations can be written in residual form and sovled with Newton/Raplson method (Xiong, 2015).

Vapor-Liquid Equilibrium Calculation

Vapor-liquid equilibrium (VLE) calculation is required in compositional model in order to obtain the phase composition and thermodynamic properties. This section discusses the VLE calculation method involving the effect of capillary pressure and/or geomechnics. In addition, the Eagle Ford tight oil is taken as the example to illustrate the VLE calculation procedure and the non-negligible effect of capillary pressure on it.

VLE Calculation with Capillary Pressure

Because of the assumption of no mass transfer between water and hydrocarbon phases, a two-phase (oil and gas) equilibrium calculation is required to obtain the phase composition and finally to evaluate the general compositional model. In a multi-component system under vapor-liquid equilibrium, the chemical potential μ of each component i throughout all co-existing phases should be equal.

$$\mu_i^o=\mu_i^g \qquad i=1,\ldots,n_c \tag{25}$$

This general requirement becomes a practical engineering tool if the chemical potential can be related to measurable or calculable quantities, such as fugacity f (Danesh, 1998) as follows.

$$f_i^o=f_i^g \qquad i=1,\ldots,n_c \tag{26}$$

The practical way to calculate fugacity of each component is to evaluate the dimensionless fugacity coefficient, Φ, which is defined as the ratio of fugacity to partial pressure of the corresponding phase for component i:

$$\Phi_i^o=\frac{f_i^o}{x_iP^o} \qquad \Phi_i^g=\frac{f_i^g}{y_iP^g} \qquad i=1,\ldots,n_c \tag{27}$$

The fugacity coefficient then can be calculated because it can be related rigorously to measurable properties, such as pressure, temperature and volume, with thermodynamic relations below (Danesh, 1998).

$$ln\Phi_i=\frac{1}{RT}\int_V^\infty\left[\left(\frac{\partial P}{\partial N_i}\right)_{T,V,N_{j\neq i}}-RT/V\right]dV-\ln Z \tag{28}$$

Equation (24) can be determined with the aid of an Equation of State (EOS), relating pressure, temperature, volume and compositions. In this paper, Peng-Robinson (Peng and Robinson, 1976) Equation of State (PR EOS) is used to evaluate lnΦ.

In addition to the above method to calculate fugacity for the conditions of VLE, the method to calculate composition of each phase at the condition of VLE is also required. A general method is to solve

Rachford-Rice (R-R) equation below (Rachford and Rice, 1952) with the input of equilibrium ratio K of component i, defined as $K_i = y_i/x_i$.

$$\sum_{i=1}^{n_c} \frac{z_i(K_i - 1)}{\tilde{n}_o + K_i(1 - \tilde{n}_o)} = 0 \tag{29}$$

In the non-ideal system at equilibrium, K_i is usually related to fugacity coefficient by combining of Equation (22) and (23) as follows.

$$(f_i^o = \Phi_i^o x_i P^o) = (f_i^g = \Phi_i^g y_i P^g) \Rightarrow K_i = \frac{y_i}{x_i} = \frac{P^o \Phi_i^o}{P^g \Phi_i^g} = \frac{P^o \Phi_i^o}{(P^o + P_{cgo})\Phi_i^g} \tag{30}$$

In conventional reservoirs, Equation (26) is simplified to $K_i = \Phi_i^o/\Phi_i^g$ by assuming that P^o equals P^g. However, this assumption is not valid for tight oil reservoirs due to large capillary pressure P_{cgo}. With capillary pressure term included in Equation (26), the effect of capillary pressure on VLE can be quantitatively evaluated. The next section takes Eagle Ford tight oil within small pores as an example to illustrate the effect capillary pressure on VLE and fluid properties.

Bubble-point Calculation with Capillary Pressure

Bubble-point pressure is the pressure at which the first gas bubble forms in oil phase. It poses two conditions at saturation pressure: oil composition is the same as the overall composition; and phases are at equilibrium. From the phase equilibrium condition, there are the following relations.

$$\sum_{i=1}^{n_c} y_i = \sum_{i=1}^{n_c} \frac{f_i^g}{\Phi_i^g P^g} = \sum_{i=1}^{n_c} \frac{f_i^o}{\Phi_i^g P^g} = 1 \tag{31}$$

From the above equation, there are also the following relations:

$$\sum_{i=1}^{n_c} \frac{f_i^o}{\Phi_i^g} = \sum_{i=1}^{n_c} \frac{\Phi_i^o x_i P^o}{\Phi_i^g} = P^g = P^o + P_{cgo}(x_i, y_i) \tag{32}$$

where p_{cgo} is the capillary pressure between oil and gas phases, which is also a function of phase composition x_i, y_i. Finally, we obtain the following iterative relation for bubble-point pressure:

$$P_{iter+1}^o = P_{iter}^o \sum_{i=1}^{n_c} \frac{\Phi_i^o x_i}{\Phi_i^g} - P_{cgo}(x_i, y_i) = P_{iter}^o \sum_{i=1}^{n_c} \frac{\Phi_i^o z_i}{\Phi_i^g} - P_{cgo}(x_i, y_i \tag{33}$$

where *iter* is the iterative step to solve the saturation pressure; Φ_i^o and Φ_i^g can be evaluated with the aid of PR-EOS.

VLE Calculation Example - Eagle Ford Tight Oil

In this example, the Young-Laplace method is used and interfacial tension is calculated with Macleod-Sugden correlation (Danesh, 1998; Weinaug and Katz, 1943). Tables 2 and 3 list the composition data and thermodynamic properties of components of the sample oil of Eagle Ford tight reservoir (Orangi et al., 2011).

Table 2—Composition and component properties of Eagle Ford tight oil (Orangi et al., 2011)

Component	Molar Fraction	p_c (psi)	T_c (°R)	v_c (ft^3/lbmole)	Acentric Factor	Molar Weight
C1	0.31231	673.1	343.3	1.5658	0.013	16.04
N2	0.00073	492.3	227.2	1.4256	0.04	28.01
C2	0.04314	708.4	549.8	2.3556	0.0986	30.07
C3	0.0414S	617.4	665.8	3.2294	0.1524	44.1
CO_2	0.01282	1071.3	547.6	1.5126	0.225	44.01
IC4	0.0135	529.1	734.6	4.2127	0.1848	58.12
NC4	0.03382	550.7	765.4	4.1072	0.201	58.12
IC5	0.01805	483.5	828.7	4.9015	0.2223	72.15
NC5	0.02141	489.5	S45.6	5.0232	0.2539	72.15
NC6	0.04623	439.7	914.2	5.9782	0.3007	86.18
C7+	0.16297	402.8	1065.5	7.4093	0.3739	114.4
C11+	0.12004	307.7	1223.6	10.682	0.526	166.6
C15+	0.10044	241.4	1368.4	14.739	0.6979	230.1
C20+	0.07306	151.1	1614.2	26.745	1.0456	409.2

Table 3—Binary interaction parameters of Eagle Ford oil (Orangi et al., 2011)

	Cl	N2	C2	C3	CO_2	IC4	NC4	IC5	NC5	NC6	C7+	C11+	C15+	C20+
Cl	0	0.036	0	0	0,1	0	0	0	0	0	0.025	0.049	0.068	0,094
N2	0.036	0	0.05	0,08	-0.02	0.095	0.09	0.095	0.1	0.1	0.151	0.197	0.235	0.288
C2	0	0.05	0	0	0,13	0	0	0	0	0	0.02	0.039	0.054	0,075
C3	0	0.08	0	0	0,135	0	0	0	0	0	0.015	0.029	0.041	0.056
CO_2	0.1	-0,02	0,13	0,135	0	0.13	0.13	0.125	0.125	0.125	0.11	0.097	0.085	0,07
IC4	0	0.095	0	0	0,13	0	0	0	0	0	0.01	0.019	0.027	0.038
NC4	0	0.09	0	0	0,13	0	0	0	0	0	0.01	0.019	0.027	0.038
IC5	0	0.095	0	0	0,125	0	0	0	0	0	0.005	0.01	0.014	0,019
NC5	0	0.1	0	0	0,125	0	0	0	0	0	0.005	0.01	0.014	0,019
NC6	0	0,1	0	0	0,125	0	0	0	0	0	0	0	0	0
C7+	0.025	0.151	0-02	0,015	0,11	0.01	0.01	0.005	0.005	0	0	0	0	0
C11+	0.049	0.197	0.039	0.029	0.097	0.019	0.019	0.01	0.01	0	0	0	0	0
C15+	0.068	0.235	0.054	0-041	0.085	0.027	0.027	0.014	0.014	0	0	0	0	0
C20+	0.094	0.288	0.075	0.056	0,07	0.038	0.038	0.019	0.019	0	0	0	0	0

Figure 4(a) presents the calculated bubble-point pressure for the oil sample in three scenarios. without effect of capillary pressure, with effect of capillary pressure in 20 nm pore radius and 10 nm pores radius. It shows that the bubble-point pressure is suppressed due to capillary pressure, especially, in the lower and middle temperature range. In the high temperature range, the difference of bubble-point pressure caused by capillary pressure is small, because it is close to the critical point, where there is no phase difference and interfacial tension becomes zero. The effect of capillary pressure on saturation pressure also results in more light components dissolved in oil phase at the pressure below bubble-point, because those light components evolves into gas phase at a lower pressure. Figure 4(b) shows the molar fraction of light components, C_1 and C_2, in oil phases under different pore radius at pressure of 1,200 psi and 1,500 psi, both below saturation pressure.

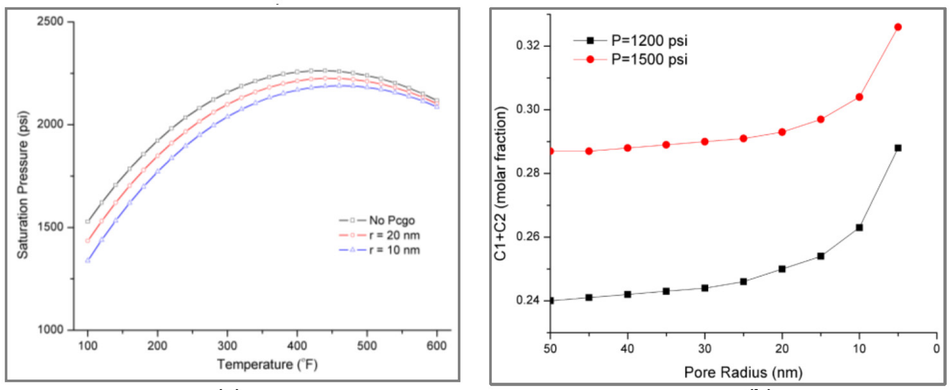

(a) (b)

Figure 4—(a) Bubble-point pressure without capillary pressure and within 10 and 20 nm nano-pores (b) Molar fraction of light components in oil phase as function of pore radius

The effect on composition of oil phase further leads to the influence on fluid properties, such as oil density and viscosity. The light components in oil phase lead to lighter oil density and smaller viscosity shown in Figure 5, where the viscosity is calculated with with Lohrenz-Bray-Clark (LBC) correlation (Lohrenz et al., 1964). The oil density and viscosity at 1,200 psi and 1,500 psi decrease as pore radius decrease due to an increase of capillary pressure.

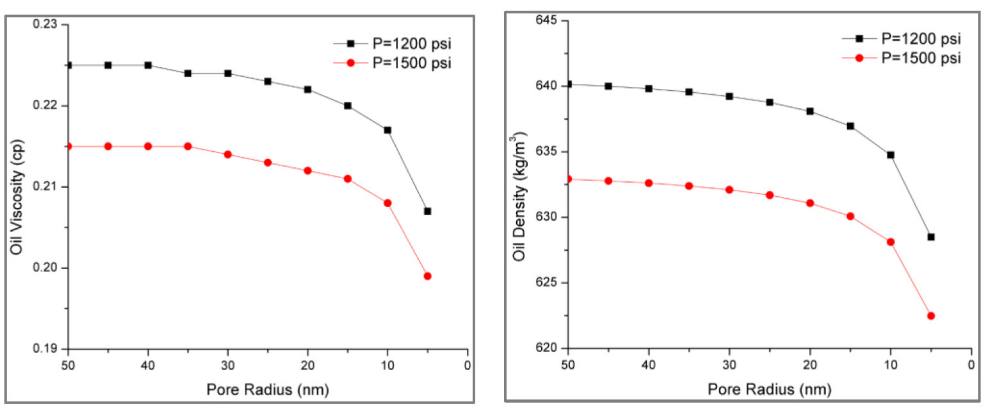

(a) (b)

Figure 5—Oil viscosity (a) and density (b) under capillarity effect

Simulation Examples - Bakken Tight Oil Reservoirs

Two simulation examples are presented in this section. The first example shows a single-porosity porous medium to demonstrate the effects of geomechanics and large capillarity on fluid flow, fluid composition, and hydrocarbon recovery of matrix rocks in tight oil reservoirs. The second example extends the simulation from a porous medium to a double-porosity fractured reservoir. The rock and fluid data of Bakken tight oil reservoirs are used in the two examples. Tables 4 and 5 show the composition data and thermodynamic properties of the Bakken oil sample in the simulation examples.

Table 4—Composition and component properties of Bakken tight oil (Nojabaei et al., 2013)

Component	Molar Fraction	P_c (MPa)	T_c (K)	MW (kg/kgmol)	Acentric factor	v_c (m^3/kgmol)	Diffusivity (m^2/s)
C_1	0.36736	4.599	190.56	16.04	0.0115	0.0986	2.8×10^{-7}
C_2	0.14885	4.872	305.32	30.07	0.0995	0.1455	2.5×10^{-7}
C_3	0.09334	4.248	369.83	44.10	0.1523	0.2000	1.9×10^{-7}
C_4	0.05751	3.796	425.12	58.12	0.2002	0.2550	1.6×10^{-7}
C_5-C_6	0.06406	3.181	486.38	78.30	0.2684	0.3365	1.2×10^{-7}
C_7-C_{12}	0.15854	2.505	585.14	120.56	0.4291	0.5500	1.2×10^{-7}
C_{13}-C_{21}	0.0733	1.721	740.05	220.72	0.7203	0.9483	1.0×10^{-7}
C_{22}-C_{80}	0.03704	1.311	1024.72	443.52	1.0159	2.2474	0.9×10^{-7}

Table 5—Binary interaction parameters of Bakken tight oil (Nojabaei et al., 2013)

	C_1	C_2	C_3	C_4	C_5 - C_6	C_7 - C_{12}	C_{13} - C_{21}	C_{22} - C_{80}
C_1	0.0	0.005	0.0035	0.0035	0.0037	0.0033	0.0033	0.0033
C_2	0.005	0	0.0031	0.0031	0.0031	0.0026	0.0026	0.0026
C_3	0.0035	0.0031	0	0	0	0	0	0
C_4	0.0035	0.0031	0	0	0	0	0	0
C_5-C_6	0.0037	0.0031	0	0	0	0	0	0
C_7 - C_{12}	0.0033	0.002G	0	0	0	0	0	0
C_{13} - C_{21}	0.0033	0.0026	0	0	0	0	0	0
C_{22} - C_{80}	0.0033	0.0026	0	0	0	0	0	0

Numerical Studies on Matrix Rocks

This example describes a tight matrix rock with 30 m × 10 m in x and y directions with 1 m thickness as shown in Figure 6, assuming that left side of the matrix is open to produce, e.g. connected to fractures. This simulation is to reproduce a laboratory core test for capturing fluid flow in tight matrix with compositional analysis involving the effects of geomechanics and capillarity on VLE.

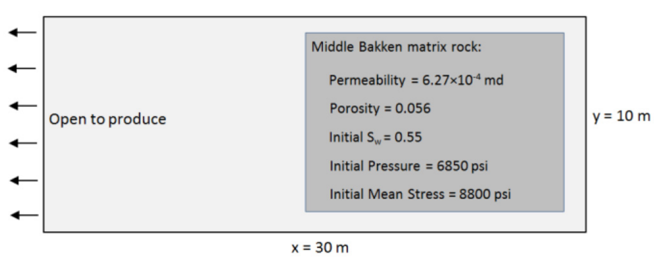

Figure 6—Oil viscosity (a) and density (b) under capillarity effect

Initially, the matrix is filled with water and oil at undersaturated condition. Kurtoglu et al. (2014) investigated rock and fluid properties of middle Bakken formation and measured moderate permeability to be 6.27×10^{-4} md. They also reported residual water and oil saturations as 0.531 and 0.211, respectively. Yu et al. (2014) estimated matrix porosity of middle Bakken formation to be 0.056 and pore compressibility to be 1×10^{-6} psi^{-1} through history matching of numerical simulations. In addition, the geomechanical properties of middle Bakken formation have been intensively investigated by researchers. Yang et al. (2013) tested middle Bakken core for Young's modulus and Poisson's ratio. He and Ling (2014) determined Biot's coefficients of a large range of Bakken samples with a new proposed method. Table 6 lists the simulation input data taken from the published sources.

Table 6—Input parameters of Bakken matrix simulation

Parameter	Value	Unit
Rock properties		
Permeability	6,19 × 10^{-19} (6.27 × 10^{-4})	m^2 (md)
Porosity	0.056	
Rock compressibility	1.45 × 10^{-10} (1 × 10^{-6})	Pa^{-1} (psi^{-1})
Young's modulus	26 (3.77 × 10^6)	GPa (psi)
Poisson's ratio	0.25	
Biot's coefficient	0.68	
Brook-Corey pore size distribution index	1.0	
Fluid properties		
Water density at standard condition	1,000.0 (62.4)	kg/m^3 (lb/ft^3)
Water viscosity	1.139 × 10^{-3} (1.139)	Pa.s (cP)
Klinkenberg coefficient	8.6 × 10^5 (125)	Pa (psi)
Residual water saturation	0.531	
Irreducible oil saturation	0.211	
Critical gas saturation	0.01	
Initial and boundary conditions		
Initial pore pressure	47.23 (6,850)	MPa (psi)
Initial mean stress	60.67 (8,800)	MPa (psi)
Stress boundary	X = 30 m	
Reservoir temperature	115 (239)	°C (°F)
Initial water saturation	0.55	
Production pressure 0 – 13.5 years	18.62 (2,700)	MPa (psi)
Production pressure 13.5 – 40.5 years	10.34 (1,500)	MPa (psi)

The initial reservoir pressure is usually very high in tight oil reservoirs, far above saturation pressure. In this case, the initial pore pressure is 6,850 psi, much higher than initial bubble-point pressure. Thus this simulation and discussions are performed in two parts: under-saturated and saturated production. In the first part, the production pressure is set to be 2,700 psi, above bubble-point, and 13.5 years (5,000 days) production is simulated. Then the production pressure is set to be 1,500 psi and another 27 years (10,000 days) simulation is performed, shown in the section of "initial and boundary condition" of Table 6. In the total 40.5 years (15,000 days) simulation, the geomechanical influences are observed in both first and second periods; while the effect of capillary pressure on VLE, only exists during under-saturated production where gas phase appears coexisting with oil phase.

Geomechanical Effect at Under-saturated Condition To demonstrate geomechanical effect on the oil production of tight formations, two simulation runs, with and without stress coupling, are performed at under-saturation condition, as shown in Figure 7. In this simulation, rock porosity is correlated with effective stress with a relationship derived by McKee et al. (1988) from hydrostatic poroelasticity theory. On the other hand, Mokhtari et al. (2013) also found that the exponential coefficient of permeability decrease is between −0.0002 to −0.0006 for unfractured tight rock in psi^{-1} unit. Thus this simulation takes exponential correlation between absolute permeability and change of effective stress with estimated coefficient −0.0003.

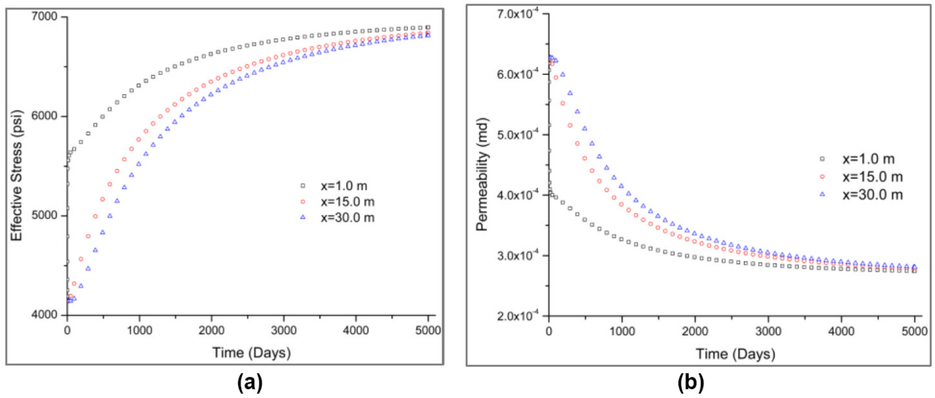

Figure 7—Effective stress evolution and induced change of permeability at under-saturated condition

Figure 6 shows the simulation results of effective stress at three different locations of the matrix sample and the absolute permeability induced by the change in effective stress. The location of $x = 1.0$ m is adjacent to the production side; $x = 15.0$ m is in the middle and $x = 30.0$ m is at the end of matrix rock. The effective stress at $x = 1.0$ m quickly increases due to fluid depletion and resulting pore pressure decrease. Similarly the effective stress at the middle and end of matrix also increases during the production, but much slower. The increase of effective stress is about 3,000 psi (approximately from 4,000 psi to 7,000 psi in Figure 6(a)). The effect of change of effective stress on absolute permeability is shown in Figure 6(b), and the permeability evolution generally follows the trend of effective stress.

Effect of Capillary Pressure on VLE During the saturation production starting from the 5,000th day, the gas phase forms at reservoir condition. The Young-Laplace equation (Equation (18)) is used to calculate the capillary pressure between oil and gas phase by assuming contact angle is zero. The interfacial tension between oil and gas phase is calculated with phase composition data and Parachor values of each component. Ayirala and Rao (2006) claim that the measured interfacial tensions are two to three times greater than those calculated with Macleod and Sugden correlation (Equation (19)) at moderate pressures; Nojabaei et al. (2013) uses three times of interfacial tension calculated with Equation (19) in the study of Bakken tight oil simulation. Thus a similar correction is taken in this study to correct the underestimated interfacial tension. The stress effect on capillary pressure is included by using the relationship between pore radius and rock porosity and permeability assuming that initial pore radius is about 30 nm.

As discussed before, the capillary pressure could postpone the appearance of gas phase, lowering bubble-point pressure, and affect the thermodynamic properties of oil and gas phases through its effect on VLE calculations. Eventually it influences the production performance. Figure 8 shows the simulation results of gas saturation at three locations of $x = 1.0$, 15.0 and 30.0 m. The gas saturation at all three locations is lower with capillarity effect on VLE. The gas saturation at $x = 1.0$ m quickly increases due to fluid depletion resulting pressure decrease. It is noted that the gas saturation at $x = 1.0$ m reaches a peak quickly and then decrease at beginning of production shown in Figure 8(a). It's because the formed gas at this location flows fast to surface and there is no sufficient gas formed in rest area to charge the gas production due to slow pressure propagation in ultra-low permeability rock. The comparison of gas saturation at $x = 15.0$ and $x = 30.0$ m demonstrates the postponed appearance of gas phase with the effect of capillary pressure on VLE. For example, the first gas bubble comes out at $\times = 15.0$ at approximate 5,600 day in Run2-1 and 5,200 day in Run2-2, about 400 days postpone shown in Figure 8(b). Similarly there is about 600 days delayed appearance of gas phase at $x = 30.0$ shown in Figure (c).

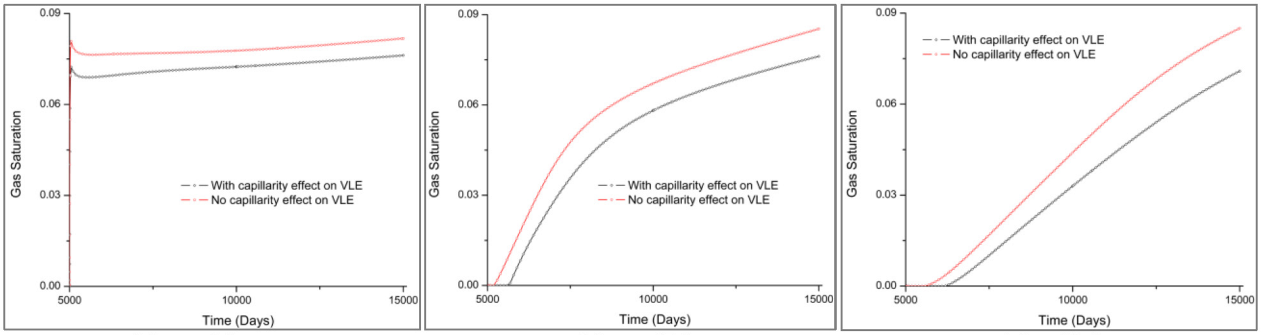

(a) x = 1.0 m **(b) x = 15.0 m** **(c) x=30.0 m**

Figure 8—Gas saturation at three locations

The higher gas saturation in reservoir condition could lead to more light components transported in gas phase and therefore produced to the surface. In order to facilitate compositional analysis, C_1 and C_2 components are categorized as light components; C_3, C_4 and C_5-C_6 are categorized as intermediate components; C_7-C_{12}, C_{13}-C_{21} and C_{22}-C_{80} are categorized as heavy components in the following discussions. Figure 9 shows the molar fraction comparison of surface production. It is observed that there is larger molar fraction of light components produced in the case without capillarity effect; the simulation run, including capillarity effect on VLE, has large molar fraction of intermediate and heavy components produced. Since less molar fraction of light components and more molar fraction of intermediate and heavy components are produced to surface with capillarity effect, the molar fractions in the reservoir condition are also different. Figure 10 presents the comparisons of simulation results for the overall molar fraction in oil and gas phases at location $\times = 15.0$ m. In the reservoir condition, simulation run with capillarity effect on VLE has more molar fraction of light components and less molar fraction of intermediate and heavy components.

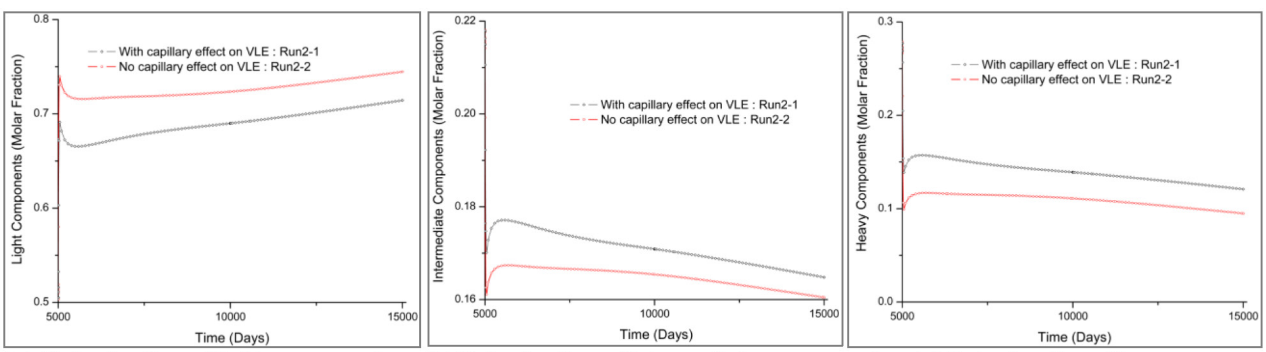

(a) Molar fraction of light components **(b) Molar fraction of intermediate components** **(c) Molar fraction of heavy component**

Figure 9—Composition comparison of surface production

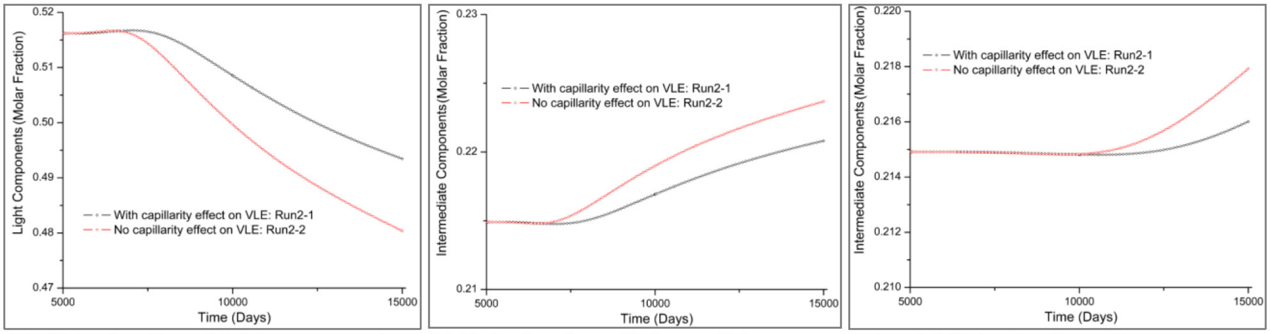

(a) Molar fraction of light components (b) Molar fraction of intermediate components (c) Molar fraction of heavy component

Figure 10—Composition comparison at reservoir condition (x = 15.0 m)

The simulated reservoir pressures are presented in Figure 11, showing the pressure evolutions at x = 1.0, 15.0, and 30.0 m. The simulation run, without capillarity effect on VLE, has higher reservoir pressure than that in Run2-1 except at x = 1.0 m, where the pressure is very close to the production pressure. The difference of simulated reservoir pressures can be explained by the differences of appearance of gas phase and corresponding gas saturation. The postponed appearance of gas phase and less gas saturation lead to faster pressure decrease.

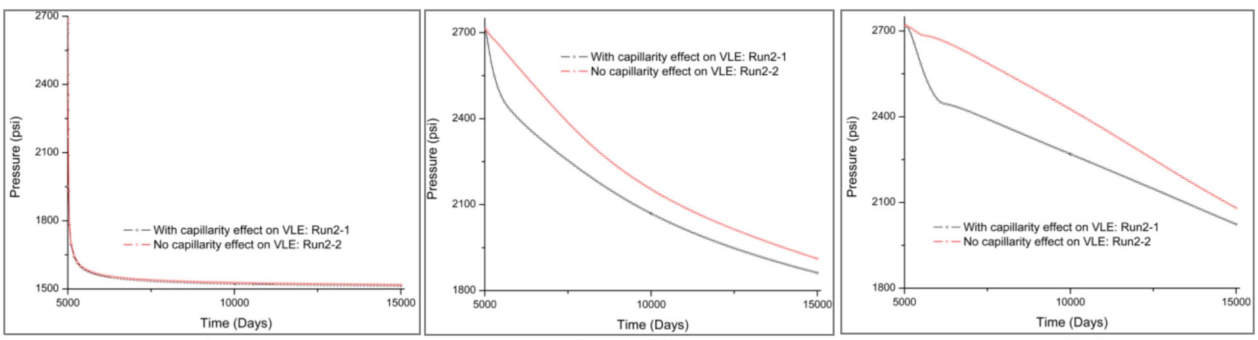

(a) x = 1.0 m (b) x = 15.0 m (c) x = 30.0 m

Figure 11—Reservor pressure evolution at three locations

The above differences of simulation results on gas saturation, reservoir and surface composition, and reservoir pressure are due to the effect of capillary pressure between oil and gas phases on their phase equilibrium. This effect can be observed from Figure 12, showing the comparison of oil phase composition at equilibrium as function of reservoir pressure. Before reservoir pressure decreases to the saturation pressure, two simulation runs have the same and constant oil composition in reservoir condition as the overlap curves in Figure 12 from initial reservoir pressure to approximate 2,500 psi. Once reservoir pressure decreases to bubble-point, the molar fraction of light components decreases, and molar fractions of intermediate and heavy components increase. The difference of phase transition point in Figure 12 shows that bubble-point pressure in the case of including capillarity effect on VLE is about 200 psi lower than the case without capillarity effect. For the same reservoir pressure below bubble point, there are more light components, but less intermediate and heavy components in oil phase due to capillarity effect on VLE.

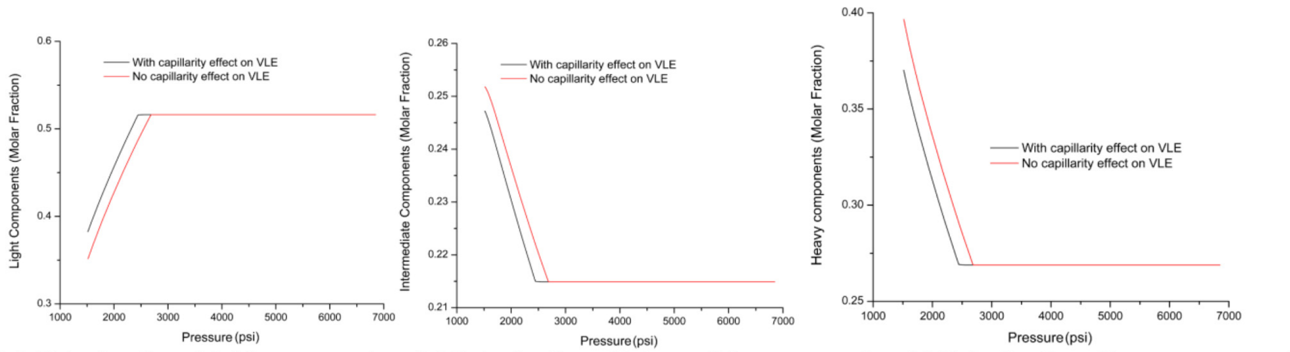

(a) Molar fraction of light components (b) Molar fraction of intermediate components (c) Molar fraction of heavy component

Figure 12—Oil phase composition as a function of reservoir pressure

Geomechanical Effect at Saturated Condition Figure 13 presents the oil composition as function of reservoir pressure for three difference scenarios. no capillarity effect on VLE, with capillarity effect on VLE only, with both capillarity and geomechanics effects. The capillary pressure between oil and gas phases is higher for the case including geomechanics effect, due to increase in effective stress affecting pore radius. This higher capillary pressure further suppresses bubble-point, therefore, Figure 13 shows there more light components and less intermediate and heavy components in oil phase than in other two cases.

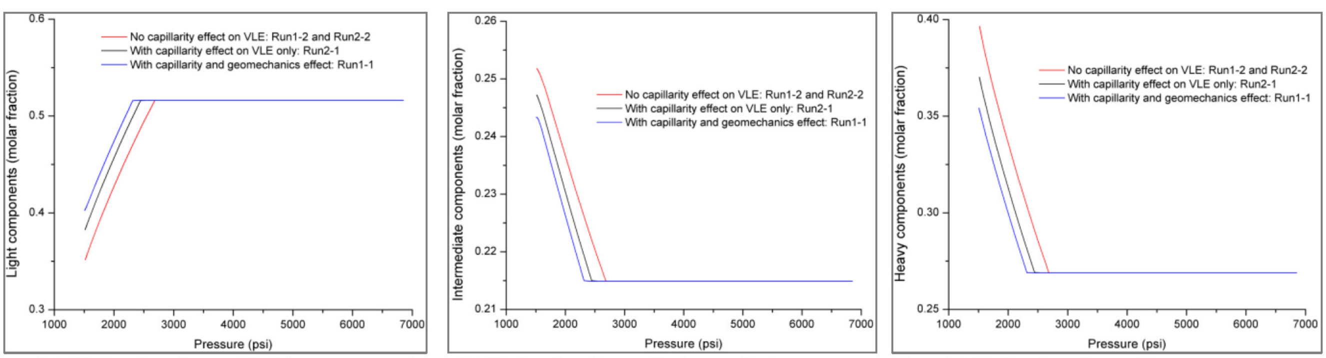

(a) Molar fraction of light components (b) Molar fraction of intermediate components (c) Molar fraction of heavy component

Figure 13—Oil phase composition as a function of reservoir pressure

The geomechanical effect leads to higher capillarity pressure, and accordingly there is larger effect on VLE calculations, which explains the comparison in Figure 13. Figure 14 shows the difference of capillary pressure induced by the change of effective stress at x = 1.0, 15.0 and 30.0 m. The capillary pressure without geomechanical effect is between 90 and 160 psi, and it increases to between 150 and 190 psi, due to stress-induced decrease of pore radius.

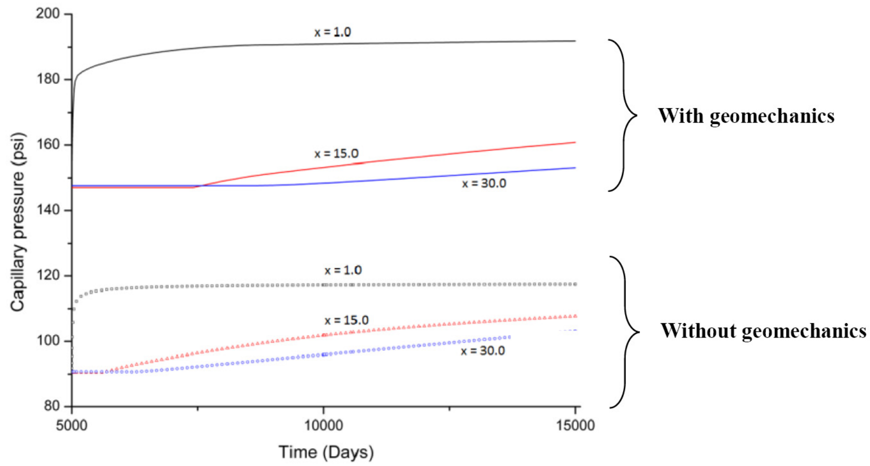

Figure 14—Values of capillary pressure involved in VLE calculation

In addition to geomechanical effect on capillary pressure, the capillarity effect on VLE also influences the computation of effective stress. As presented in Figure 11 of previous section, the reservoir pressure is different between the cases with capillarity effect on VLE and without this effect, because higher gas saturation in reservoir in the case without capillarity effect on VLE leads to higher reservoir pressure. Consequently it affects the effective stress. Figure 15 shows the comparison of simulated effective stress. The case including capillarity effect on VLE has higher effective stress due to its lower reservoir pressure.

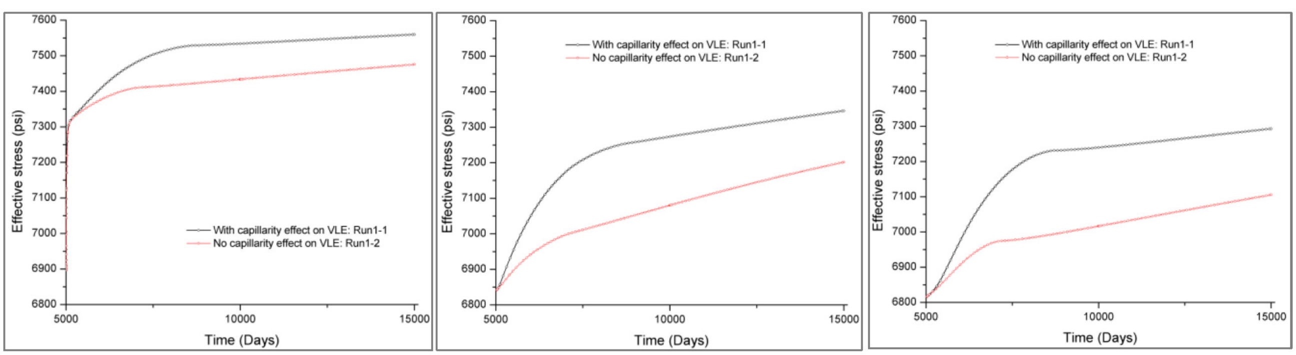

Figure 15—Effective stress comparison between with and without capillarity effect

The accumulated production during saturated production is also compared for all four scenarios, shown in Figure 16. The accumulated production of oil and gas in the cases with geomechanical effect, are less than the cases without geomechanical effect, because the absolute permeability decreases due to increase of effective stress. And the capillarity effect on VLE favors more liquid but less gas productions.

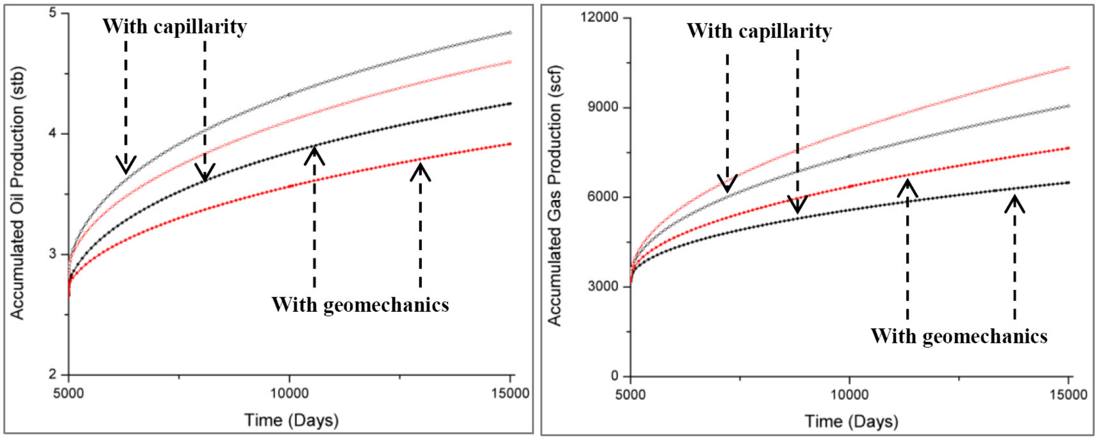

Figure 16—Comparison of accumulated oil and gas production under effects of capillarity and geomechanics

Capillarity Effect on a Fractured Reservoir

This section presents a modeling study of a tight oil reservoir with horizontal production well and multistage hydraulic fractures. Mayerhofer et al. (2010) introduced the concept of stimulated reservoir volume (SRV) to describe the size of created or enhanced fracture network by hydraulic fracturing. In this simulation example, an optimal case for creating SRV is considered where all the areas between hydraulic fractures are activated as fracture network. Figure 17 shows the schematic diagram of the full reservoir system, including a horizontal well, three-stage hydraulic fractures, and natural fractures within SRV and outside SRV. The natural fractures in SRV is enhanced by hydraulic fracturing, thus we distinguish the natural fractures as macro-fractures and micro-fractures within and outside SRV. Table 7 summerizes the reservoir properties for different types of rocks and fracturs.

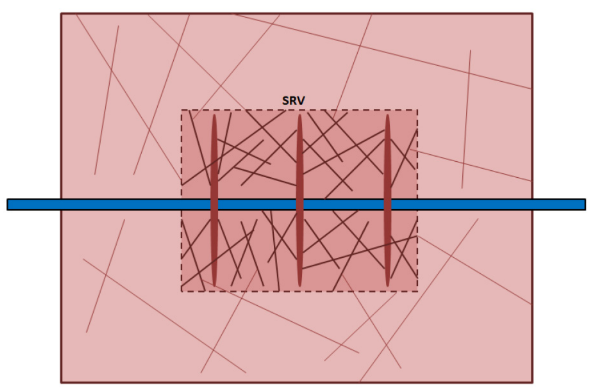

Figure 17—Schematic diagram of full reservoir: horizontal well, hydraulic fractures, and natural fractures within and outside SRV

Table 7—Reservoir properties for different types of rocks

Properties	Value	Unit
Hydraulic fractures		
Permeability	3.95×10^{-12} (4.0×10^{3})	m^2 (md)
Porosity	0.5	
Macro-fractures		
Permeability	$9.87 \times 10\text{-}^{16}$ (1.0)	m^2 (md)
Porosity	0.002	
Micro-fractures		
Permeability	$9.87 \times 10\text{-}^{17}$ (0.1)	m^2 (md)
Porosity	0.002	
Residual saturations of fracture rock		
Critical gas saturation	0.01	
Residual water saturation	0.30	
Residual oil saturation	0.05	
Matrix rock		
Permeability	$2.96 \times 10\text{-}^{19}$ ($3.0 \times 10\text{-}^{4}$)	m^2 (md)
Porosity	0.056	
Critical gas saturation	0.01	
Residual water saturation	0.531	
Residual oil saturation	0.211	

Since the effect of capillary pressure only exists during the production with reservoir pressure below saturation pressure, a constant production pressure is set to 1,500 psi, below saturation pressure, in this simulation. It is also assumed that the reservoir has been depleted for some time; the current pressure (initial pressure of this simulation) is 3,000 psi. A total 60 years simulation is performed in this study so that the reservoir is fully drained at 1,500 psi production pressure. Two simulation runs, with and without effect of capillary pressure on VLE, are performed and the simulation results are compared in this section. And the effect of capillary pressure on VLE is only considered for matrix rocks. Figure 18 and 19 shows the gas saturation contiour diagram after 1 day and 10 year production.

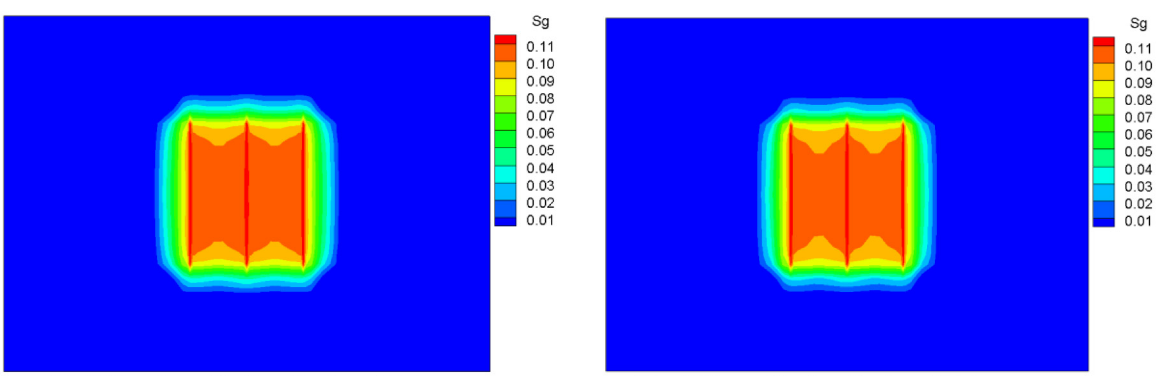

(a) Without capillarity effect on VLE (b) With capillarity effect on VLE

Figure 18—Gas saturation of fracture continuum after 1 day production (no gas formed in matrix continnum)

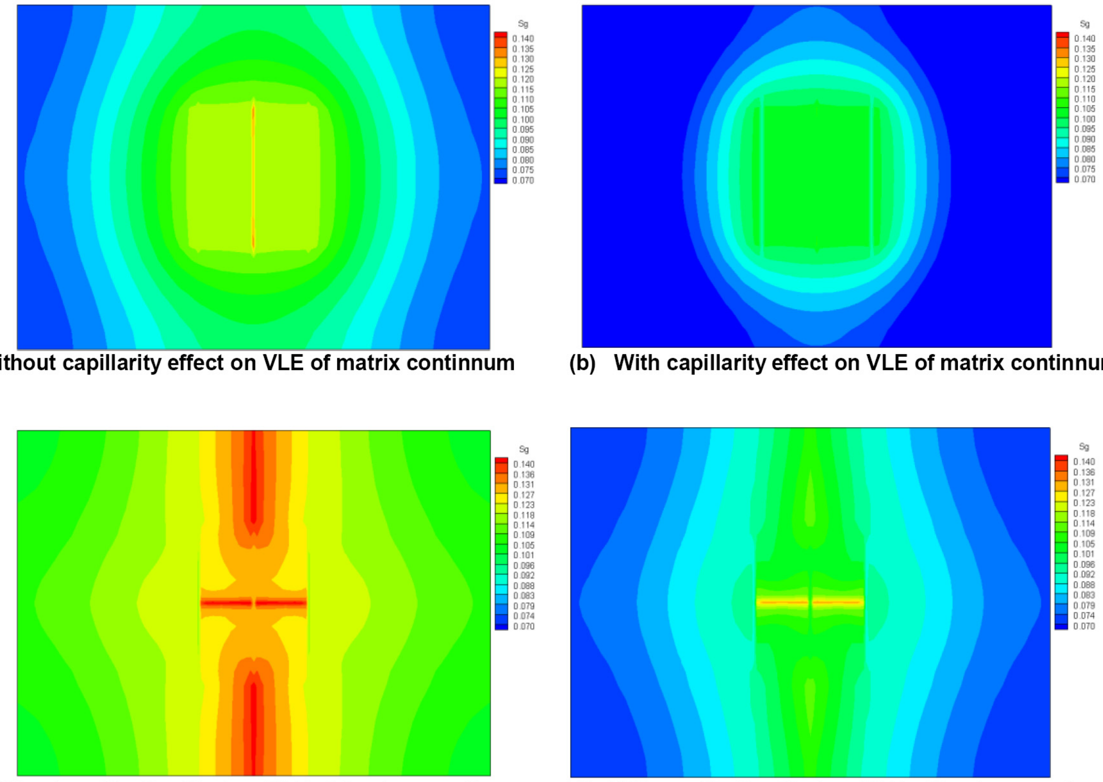

(a) Without capillarity effect on VLE of matrix continnum (b) With capillarity effect on VLE of matrix continnum

(c) Without capillarity effect on VLE of fracture continnum (d) With capillarity effect on VLE of fracture continnum

Figure 19—Reservoir gas saturation after 10 years production

At the very beginning of the simulation, the depletions are mainly from fracture continuum; thus the effect of capillary pressure on flow behaviors cannot be observed in Figure 18. The capillary effect is observed as the production continues and reservoir pressure, especially, matrix pressure decreases below bubble point. One of the main observed characteristics in the simulation runs with capillarity effect is the lower gas saturation due to suppressed saturation pressure. Figure 19 presents the comparison of gas saturation at the end of 10 year simulation in both fracture and matrix systems. The capillarity effect on VLE is observed in both matrix and fracture continua, where gas saturation is lower due to capillarity effect on VLE.

Figure 20 shows the production performance with capillarity effect on VLE. The oil rate decreases fast at the early stage of the production, when the production is mainly from fractures and the two cases have the same production rate during this time (from beginning to about 0.01 year). The oil production rate in the case with capillarity effect is always higher after about 5 years production, as shown Figure 20 (a). However, there is some time (from 0.3 – 7 years) when the oil rate in the case without capillarity effect is higher; because the solution gas comes out earlier in the case with no capillarity effect and it helps the oil production; as more gas comes out and gas saturation reaches critical gas saturation, the oil production decreases. The difference of oil production is also observed in the accumulated oil production in Figure 20 (b), which shows about 27 MSTB and 25 MSTB oil recoveries in the two cases. Figure 20(c) presents the accumulated gas production and producing gas oil ratio. It clearly shows that there are much more gas produced in the case without capillarity effect, 89 MMSCF compared 67 MMSCF. It is also noted that the gas oil ratio at very early time increases to about 7,000 scf/stb and then quickly decreases to about 1,500 scf/stb before steadily increases, which is due to the early production from fracture rock.

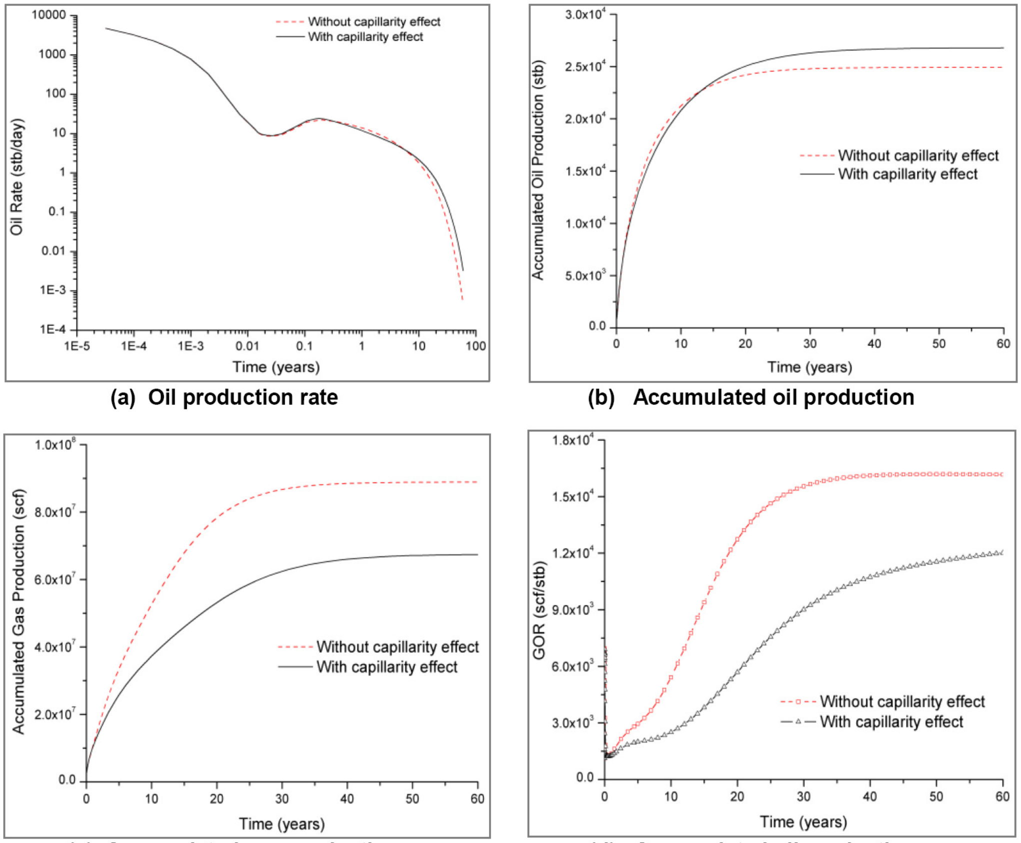

(a) Oil production rate (b) Accumulated oil production

(c) Accumulated gas production (d) Accumulated oil production

Figure 20—Production performance with capillarity effect on VLE for a double-porosity reservoir

Conclusions

This paper presents a multiphase, multidimensional compositional numerical reservoir model, fully coupled with geomechanics, to capture the effect of large capillary pressure on flow and transport in unconventional reservoirs. The phase bahavor for the compositional model is evaluated using Peng-Robinson Equation of State, including the impact of capillary pressure or geomechnics. As application examples of the proposed model, we conduct a series of modeling studies using the data from Bakken tight oil formations. The following conclusions can be drawn from our simulation results:

1. The oil production from low permeability, tight reservoirs with very high initial pore pressure leads to substantial increase of effective stress; consequently the induced decrease in absolute permeability undermines the production performance.
2. The geomechanical effect is more prominent during the production in undersaturated condition or with reservoir pressure above oil saturation pressure than in saturated condition, because pore pressure decreases fast without gas phase presence at reservoir condition and the decrease in pressure is substantial due to very high initial pressure as well as low rock permeability.
3. The effect of capillary pressure on VLE suppresses the saturation pressure and results in more light components dissolved in the oil phase, which influences the oil properties, such as oil density and viscosity. This effect could be exaggerated due to production-induced increase of effective stress.
4. The effect of capillary pressure on VLE leads to lower gas saturation at reservoir condition, less gas and more oil production, and larger molar fraction of light components remained in reservoir.
5. The effect of capillary pressure on VLE also leads to the different evolution of reservoir pressure during the production, compared to the case without this effect. Reservoir pressure decreases a

little faster in the case with capillarity effect on VLE due to postponed gas phase appearance and lower gas saturation. This evolution difference in reservoir pressure could influence the effective stress.

6. Capillarity effect on VLE is not observed at early production under saturated condition in the double-porosity fractured reservoir, when the production is mainly from fracture continuum.
7. The capillarity effect on VLE has larger influence on suppression of gas production than on growth of oil production in the simulation case for a double-porosity reservoir.
8. The numerical studies show that the effect of capillary pressure on VLE has non-negligible influence on the production performance. However, the reliable model or experiment data for capillary pressure in nano-pores are seldom available. Thus it is recommended that more experimental and theoretical work should be pursued to build an accurate model to predict or correlate the capillary pressure in nano-pores.

Acknowledgement

The authors would like to extend thanks to Energy Modeling Group (EMG) of Petroleum Engineering Department at Colorado School of Mines and Foundation CMG for the support of this research.

Nomenclature

A	Interface area between grid blocks [ft^2]
D	Coefficient of molecular diffusion [ft^2/day]
F_b	Body force [lbf]
F	Mass flux per unit volume of reservoir [lbmol/ft^3/day]
f	Fugacity of component in oil or gas phase [psi]
G	Shear modulus [psi]
K	Equilibrium ratio of component [-]
k	Absolute permeability [md]
k_r	Relative permeability of phases [-]
N	Mass accumulation per unit volume of reservoir [lbmol/ft^3]
n_c	Total number of hydrocarbon components [-]
n_b	Total number of grid blocks [-]
$\tilde{n}$	Mole fraction of oil or gas phase over whole hydrocarbon system [-]
P	Reservoir pressure [psi]
P_c	Capillary pressure [psi]
P_σ	Parachor value [-]
q	Sink/source per unit volume of reservoir [lbmol/ft^3/day]
R	Ideal gas constant [$ft^3 psiR^{-1} lbmol^{-1}$]
S	Saturation of water, oil or gas phase [-]
T	Temperature [°F]
t	Time [days]
u	Displacement [ft]
V	Volume [ft^3]
$\vec{v}$	Darcy velocity of water, oil or gas phase [ft/day]
x	Molar fraction in oil phase [-]
y	Molar fraction in gas phase [-]
Z	Compressibility factor [-]
z	Total molar fraction in hydrocarbon system of component [-]
α	Biot coefficient [-]

β Linear thermal expansion coefficient [R^{-1}]
Φ Fugacity coefficient [-]
Φ Reservoir porosity [-]
σ Stress [psi]
ρ Molar density of water, oil or gas phase [$lbmol/ft^3$]
μ Viscosity [cP]
μ Chemical potential [psi]
ε_v Volumetric strain [-]
λ Lames constant [psi]
V Poisson's ratio [-]
Ψ Flow potential [psi]
η A set of neighboring grid blocks of a grid block [-]

Subscripts

g Gas phase
i Index of mass component
k Index of primary variables
m Mean stress
n Index of grid block
$nm+1/2$ A proper averaging at the interface between grid blocks n and m
o Oil phase
p Iteration level
w Water phase
β Fluid phase
κ Index of primary equations
0 Reference state

Superscripts

t Time step level

References

Ayirala, S. C. and Rao, D. N. (2006), 'A new mechanistic parachor model to predict dynamic interfacial tension and miscibility in multicomponent hydrocarbon systems', *Journal of colloid and interface science* **299**(1), 321–331.

Biot, M. A. (1957), 'The elastic coefficients of the theory of consolidation', *J. appl. Mech.* **24,** 594601.

Chu, L., Ye, P., Harmawan, I. S. et al(2012), Characterizing and simulating the nonstationariness and nonlinearity in unconventional oil reservoirs: Bakken application, in 'SPE Canadian Unconventional Resources Conference', Calgary, Alberta, Canada, 30 October-1 November. Society of Petroleum Engineers.

Danesh, A.(1998), PVT and phase behaviour of petroleum reservoir fluids, Vol. **47,** Elsevier.

Deloitte (2014), 'Play summaries of key north american unconventional shale and canadian coal bed methane basins'. Accessed: 2014-10-06.

EIA, U.(2013a), 'Annual energy outlook 2013', *US Energy Information Administration,* Washington, DC.

EIA, U.(2013b), 'Technically recoverable shale oil and shale gas resources: an assessment of 137 shale formations in 41 countries outside the united states', US Department of Energy/EIA, Washington, DC.

Firincioglu, T., Ozkan, E. and Ozgen, C. (2012), Thermodynamics of multiphase flow in unconventional liquids-rich reservoirs, in 'SPE Annual Technical Conference and Exhibition', San Antonio, Texas, 8-10 October.

He, J. and Ling, K. (2014), A new method to determine biot coefficients of bakken samples, in '48th US Rock Mechanics/Geomechanics Symposium', Minneapolis, Minnesota, 1-4 June. American Rock Mechanics Association.

Hu, L., Winterfeld, P. H., Fakcharoenphol, P. and Wu, Y.-S. (2013), 'A novel fully-coupled flow and geomechanics model in enhanced geothermal reservoirs', *Journal of Petroleum Science and Engineering 107,* 1–11.

Jaeger, J. C., Cook, N. G. and Zimmerman, R. (2007), *Fundamentals of rock mechanics,* fourth edn, John Wiley and Sons.

Klinkenberg, L. (1941), The permeability of porous media to liquids and gases, in 'Drilling and production practice', New York, New York, 1 January. American Petroleum Institute.

Kuila, U. and Prasad, M. (2011), Understanding pore-structure and permeability in shales, in 'SPE Annual Technical Conference and Exhibition', Denver, Colorado, 30 October-2 November.

Kurtoglu, B., Kazemi, H., Rosen, R. et al(2014), A rock and fluid study of middle bakken formation: Key to enhanced oil recovery, in 'SPE/CSUR Unconventional Resources Conference- Canada', Calgary, Alberta, Canada, 30 September – 2 October.

Lai, B. and Miskimins, J. L. (2010), A new technique for accurately measuring two-phase relative permeability under non-darcy flow conditions, in 'SPE Annual Technical Conference and Exhibition', Florence, Italy, 19-22 September.

Leverett, M. (1940), 'Capillary behavior in porous solids', *Trans. Am. Inst* **142**(01), 152–169.

Lohrenz, J., Bray, B. G. and Clark, C. R. (1964), 'Calculating viscosities of reservoir fluids from their compositions', *Journal of Petroleum Technology* **16**(10), 1171–1176.

Luneau, B., Longman, M., Kaufman, P. et al (2011), 'Stratigraphy and petrophysical characteristics of the niobrara formation in the denver basin, colorado and Wyoming', *Search and Discovery Article* (50469).

Mayerhofer, M. J., Lolon, E., Warpinski, N. R. et al (2010), 'What is stimulated reservoir volume?', *SPE Production and Operations* **25**(1), 89–98.

McKee, C., Bumb, A. and Koenig, R. (1988), 'Stress-dependent permeability and porosity of coal and other geologic formations', *SPE formation evaluation* **3**(01), 81–91.

Mokhtari, M., Alqahtani, A. A., Tutuncu, A. N. et al (2013), Stress-dependent permeability anisotropy and wettability of shale resources, in 'Unconventional Resources Technology Conference', Denver, Colorado, 12-14 August.

Narasimhan, T. and Witherspoon, P. (1976), 'An integrated finite difference method for analyzing fluid flow in porous media', *Water Resources Research* **12**(1), 57–64.

Nelson, P. H. (2009), 'Pore-throat sizes in sandstones, tight sandstones, and shales', *AAPG bulletin* **93**(3), 329–340.

Nojabaei, B., Johns, R. T. and Chu, L.(2013), 'Effect of capillary pressure on phase behavior in tight rocks and shales', *SPE Reservoir Evaluation and Engineering* **16**(03), 281–289.

Orangi, A., Nagarajan, N. R., Honarpour, M. M. et al (2011), Unconventional shale oil and gascondensate reservoir production impact of rock fluid and hydraulic fractures, in 'SPE Hydraulic Fracturing Technology Conference', The Woodlands, Texas.

Peng, D.-Y. and Robinson, D. B. (1976), 'A new two-constant equation of state', *Industrial and Engineering Chemistry Fundamentals* **15**(1), 59–64.

Pioneer Natural Resource, I. (2013), Horizontal spraberry/wolfcamp acceleration, in 'Hart Energy 2013 DUG Conference'.

Pruess, K. (1991), Tough2: A general-purpose numerical simulator for multiphase fluid and heat flow, *Technical report,* Lawrence Berkeley Lab., CA.

Rachford H.Jr, and Rice, J. (1952), 'Procedure for use of electronic digital computers in calculating flash vaporization hydrocarbon equilibrium', *Journal of Petroleum Technology* **4**(10), 327–328.

Sigmund, P., Dranchuk, P., Morrow, N. et al (1973), 'Retrograde condensation in porous media', *Society of Petroleum Engineers Journal* **13**(02), 93–104.

Terzaghi, v. K. (1936), The shearing resistance of saturated soils and the angle between the planes of shear, in 'Proceedings of the 1st international conference on soil mechanics and foundation engineering', Vol. **1,** pp. 54–56.

Wang, Y., Yan, B. and Killough, J. (2013), Compositional modeling of tight oil using dynamic nanopore properties, in 'SPE Annual Technical Conference and Exhibition', New Orleans, Louisiana, 30 September-2 October.

Weinaug, C. F. and Katz, D. L. (1943), 'Surface tensions of methane-propane mixtures', *Industrial and Engineering Chemistry* **35**(2), 239–246.

Winterfeld, P. H. and Wu, Y.-S. (2015), Simulation of THM processes in fractured reservoirs, in B. Faybishenko, S. M. Benson and J. E. Gale, eds, '*Fluid Dynamics in Complex Fractured-Porous Systems*', American Geophysical Union.

Winterfeld, P., Yin, X. and Wu, Y. (2013), Numerical simulation of thermal-hydrological- mechanical-chemical processes during co_2 geo-sequestration in saline aquifer, in 'AGU Fall Meeting Abstracts', Vol. **1,** p. 1247.

Xiong, Y. (2015), Development of a compositional model fully coupled with geomechanics and its application to tight oil reservoir simulation, PhD thesis, Colorado School of Mines, Golden, Colorado.

Xiong, Y., Fakcharoenphol, P., Winterfeld, P. et al (2013), Coupled geomechanical and reactive geochemical model for fluid and heat flow: application for enhanced geothermal reservoir, in 'SPE Reservoir Characterization and Simulation Conference and Exhibition', Abu Dhabi, UAE, 16-18 September.

Yang, Y., Zoback, M., Simon, M. et al (2013), An integrated geomechanical and microseismic study of multi-well hydraulic fracture stimulation in the bakken formation, in 'Unconventional Resources Technology Conference', Denver, Colorado, 12-14 August.

Yu, W., Lashgari, H. and Sepehrnoori, K. (2014), Simulation study of co_2 huff-n-puff process in bakken tight oil reservoirs, in 'SPE Western North American and Rocky Mountain Joint Meeting', Denver, Colorado, 17-18 April.

Zarragoicoechea, G. J. and Kuz, V. A. (2004), 'Critical shift of a confined fluid in a nanopore', *Fluid phase equilibria* **220**(1), 7–9.

Zhang, R. (2013), Numerical Simulation of Thermal Hydrological Mechanical Chemical Processes During CO_2 Geological Sequestration, PhD thesis, Colorado School of Mines, Golden, Colorado.

Zoback, M. D. (2007), Reservoir geomechanics, Cambridge University Press.